

Particle-in-cell simulations of electron acceleration from relativistic interaction of mid-infrared laser interactions with near solid density matter

Gregory K. Ngirmang, Chris Orban, Scott Feister, John T. Morrison, Enam A. Chowdhury, and W. M. Roquemore

Citation: *Physics of Plasmas* **24**, 103112 (2017); doi: 10.1063/1.4995669

View online: <http://dx.doi.org/10.1063/1.4995669>

View Table of Contents: <http://aip.scitation.org/toc/php/24/10>

Published by the *American Institute of Physics*



**COMPLETELY
REDESIGNED!**

Physics Today Buyer's Guide
Search with a purpose.

Particle-in-cell simulations of electron acceleration from relativistic interaction of mid-infrared laser interactions with near solid density matter

Gregory K. Ngirmang,^{1,2,a)} Chris Orban,^{1,2} Scott Feister,^{1,3} John T. Morrison,² Enam A. Chowdhury,^{1,4} and W. M. Roquemore⁵

¹Department of Physics, The Ohio State University, Columbus, Ohio 43210, USA

²Innovative Scientific Solutions, Inc., Dayton, Ohio 45459, USA

³Department of Astronomy and Astrophysics, University of Chicago, Chicago, Illinois 60637, USA

⁴Intense Energy Solutions, LLC., Plain City, Ohio 43064, USA

⁵Air Force Research Laboratory, Dayton, Ohio 45433, USA

(Received 13 July 2017; accepted 18 August 2017; published online 26 September 2017)

Advances in ultra-intense laser technology are enabling, for the first time, relativistic intensities at mid-infrared (mid-IR) wavelengths. Anticipating further experimental research in this domain, we present high-resolution two dimensional Particle-in-Cell (PIC) simulation results using the Large-Scale Plasma (LSP) code that explores intense mid-IR laser interactions with near solid density targets. We present the results of thirty PIC simulations over a wide range of intensities ($0.03 < a_0 < 40$) and wavelengths ($\lambda = 780 \text{ nm}$, $3 \mu\text{m}$, and $10 \mu\text{m}$). Earlier studies [Orban *et al.*, Phys. Plasmas **22**, 023110 (2015) and Ngirmang *et al.*, Phys. Plasmas **23**, 043111 (2016)], limited to $\lambda = 780 \text{ nm}$ and $a_0 \sim 1$, identified super-ponderomotive electron acceleration in the laser specular direction for normal-incidence laser interactions with dense targets. We extend this research to mid-IR wavelengths and find a more general result that normal-incidence super-ponderomotive electron acceleration occurs provided that the laser intensity is not highly relativistic ($a_0 \lesssim 1$) and that the pre-plasma scale length is similar to or longer than the laser wavelength. Under these conditions, ejected electron angular and energy distributions are similar to expectations from an analytic model used in Ngirmang *et al.* [Phys. Plasmas **23**, 043111 (2016)]. We also find that, for $a_0 \sim 1$, the mid-IR simulations exhibit a classic ponderomotive steepening pattern with multiple peaks in the ion and electron density distribution. Experimental validation of this basic laser-plasma interaction process should be possible in the near future using mid-IR laser technology and optical interferometry. © 2017 Author(s). All article content, except where otherwise noted, is licensed under a Creative Commons Attribution (CC BY) license (<http://creativecommons.org/licenses/by/4.0/>). [<http://dx.doi.org/10.1063/1.4995669>]

I. INTRODUCTION

While advances in laser technology have allowed ultra-intense laser interactions at near-infrared (near-IR) wavelengths to be thoroughly explored, it is only more recently that ultra-intense laser interactions at mid-IR wavelengths have become experimentally possible.³ A variety of groups are beginning to examine what may be learned from experiments at these wavelengths and how phenomena observed in the near-IR may scale to longer wavelengths.⁴ Some of this interest stems from the existence of atmospheric “windows” in the mid-IR,⁵ while other groups consider how the longer length scale of mid-IR interactions and lower critical density [defined in Eq. (1)] of such lasers allows subtle phenomena to be more easily probed,^{6,7} and recently, mid-IR laser filaments have been demonstrated in air.⁸ Another interesting value of intense mid-IR interactions is in examining the physics of laser damage.^{9,10}

To the best of our knowledge, despite recent interest in mid-IR ultra-intense laser interactions, the literature has not focused much attention on short-pulse, intense mid-IR laser interactions with dense (i.e., solid or liquid density) targets.

These interactions are interesting for a variety of reasons, among them is the favorable scaling of the ponderomotive electron energy with laser wavelength ($a_0 \propto \sqrt{I\lambda^2} \propto \lambda$). However, given the complexity of ultra-intense interactions with dense targets, these scaling arguments can only offer an order-of-magnitude expectation for the results of detailed simulations and experiments in this regime. With experimental capabilities still growing in the mid-IR, the present work offers a simulation survey of energetic electron ejection from mid-IR laser irradiated dense targets and may guide future experiments.

The work presented here is motivated in part by earlier investigations of normal-incidence ultra-intense laser interactions with liquid targets at the Air Force Research Lab (AFRL), which found much larger than expected conversion efficiencies from laser energy to ejected electron energy.¹¹ These experimental results prompted simulation work by Refs. 1 and 2. Orban *et al.*¹ presented 2D(3v)/Particle-in-Cell (PIC) simulations showing significant electron ejection at superponderomotive energies and emphasized that ultra-intense laser interactions at $\sim 10^{18} \text{ W cm}^{-2}$ ($a_0 \sim 1$ for $\lambda \approx 800 \text{ nm}$) intensities present in the experiment should create strong-standing wave fields near the target. Ngirmang *et al.*² performed 3D PIC simulations of these targets and

^{a)}Electronic mail: ngirmang.1@osu.edu

provided an analytic model to explain both the energies and the angular distribution of ejected electrons. More recently, Feister *et al.*¹² have reported direct experimental measurements of the ejected electron energies, confirming the existence of multi-MeV electrons in the experiment and from the reinforcing conclusions that the conversion efficiency in the experiment is large compared to other ultra-intense laser experiments. Given the promise shown in this effect, an interesting question is whether superponderomotive electron ejection occurs even with intense mid-IR laser systems. This work, therefore, investigates this acceleration mechanism over a wide parameter scan of intensities and wavelengths, including up to 10 J, 10 μm and 3 μm short-pulse lasers, a regime which encompasses state-of-the-art laser systems, such as the 15 TW CO₂ laser system at UCLA,¹³ or laser systems which are under planning or are up and coming, and Sec. II describes our simulation setup. Section III describes our results. Finally, Sec. V provides a summary and conclusions.

II. PARTICLE-IN-CELL SIMULATIONS

Intense laser-matter interactions were investigated using high-resolution 2D(3v)/PIC simulations with the Large-Scale Plasma (LSP) code¹⁴ in a parameter scan encompassing 30 simulations (see Table I for a summary and the Appendix for the precise parameters of all 30 simulations). For all simulations, the initial conditions included a liquid-density water slab target with some assumed pre-plasma scale length similar to earlier studies.^{1,2} In all simulations, a laser is normally incident onto the water slab. We use the following Cartesian coordinate system for these simulations: the positive x -axis is the direction of the laser, the y -axis is the polarization direction, and the z -axis is the axis of the water column, which is assumed to be the axis of symmetry in the 2D(3v)/PIC simulations.

The simulations involve a normally incident, spatially Gaussian, sine-squared envelope pulse with 780 nm, 3 μm , and 10 μm wavelengths (denoted λ). These simulations extend the results of earlier investigations with 780 nm laser pulses^{1,2} by examining the same phenomena with mid-infrared (IR) wavelengths. For convenience, we will often refer to the set of all simulations performed with a particular laser wavelength incident by saying, for example, “the 3 μm simulations,” and likewise for the other wavelengths. All the 780 nm simulations had a laser pulse with a 2.15 μm Gaussian radius and a 40 fs temporal full-width-half-maximum (FWHM) pulse duration (similar to the laser system described in Refs. 1, 2, and 11). The 3 μm simulations have

laser pulses with 8.25 μm Gaussian radius and 158 fs FWHM pulse duration, and the 10 μm simulations have laser pulses with 27.5 μm Gaussian radii and 510 fs. These Gaussian radii and pulse durations were chosen, so that the ratio of the wavelength to the Gaussian radius and the number of optical periods T in a pulse were fixed across all simulations, regardless of the laser wavelength. For each wavelength, we simulated a range of pulse energies from 10^{-4} J, 1 mJ, 10 mJ, 1 J to 10 J. Since the Gaussian radius and the pulse duration were fixed for each wavelength, this was done by changing the intensity. Simulation parameters for each wavelength simulation are summarized in Table I.

The target in all simulations consisted of free electrons, protons, and O⁺ ions, with number densities set in relative proportion to make the target match water’s chemical composition and ensure charge neutrality (O⁺ to p⁺ to e[−] ratio of 1:2:3). In all simulations, the plasma density only varied along the x direction. In the target region, the density is constant and in the pre-plasma region, the density profile exponentially decreases in x away from the target region.

For comparison with previous studies,^{1,2} for every intensity and wavelength considered, we performed a simulation with a 1.5 μm exponential scale-length. In addition, for 3 μm and 10 μm wavelengths, we also perform simulations where the pre-plasma scale length is a constant multiple of the wavelength ($L = 1.92\lambda$), so that we performed 3 μm simulations with a 5.77 μm scale length and 10 μm simulations with a 19.2 μm scale-length. We refer to these scale lengths as the “proportional” scale lengths. The 780 nm and 3 μm simulations had a target region electron density of 10^{23} cm^{-3} , which with the O⁺ to p⁺ to e[−] ratio mentioned earlier correspond to the mass density of 1 g/cm³, as one would expect for liquid water. The 10 μm simulations with a 1.5 μm scale length also had a target region with this same 10^{23} cm^{-3} electron density into the target. However, the 10 μm simulations with a 19.2 μm scale-length had a target region electron density of 10^{21} cm^{-3} in order to reduce the size of the target to reduce computational requirements. The 780 nm simulations used a target that was 20 μm wide in the y direction, the 3 μm simulations used a 100 μm wide target, and the 10 μm simulations used a 220 μm wide target. All targets had an initial temperature of 1 eV. All simulations had absorbing boundaries with 10 μm between the initial target and the simulation boundaries.

The non-relativistic formula for the critical electron density is

$$n_c = 4\pi m_e \omega^2 / e^2 = m_e / \pi \lambda^2 e^2. \quad (1)$$

TABLE I. Summary of parameters for each simulation with a given incident wavelength laser. As explained in Table II, the performed simulations had parameters, such as laser pulse duration and Gaussian radius, chosen to scale proportionally with the wavelength. Also explained in the referenced section is that simulations with 1.5 μm were performed for all wavelengths.

Wavelength (μm)	Intensity range (W/cm^2)	Gaussian radius (μm)	Pulse FWHM (fs)	Proportional scale-length (μm)	Simulation timestep (fs)	Simulation spatial resolution (μm)
10	1.64×10^{13} – 1.64×10^{18}	27.5	513	19.2	0.5	0.25
3	6.08×10^{14} – 6.08×10^{19}	8.5	154	5.77	0.15	0.1
0.78	3.46×10^{16} – 3.46×10^{21}	0.15	40	1.5	0.1	0.033

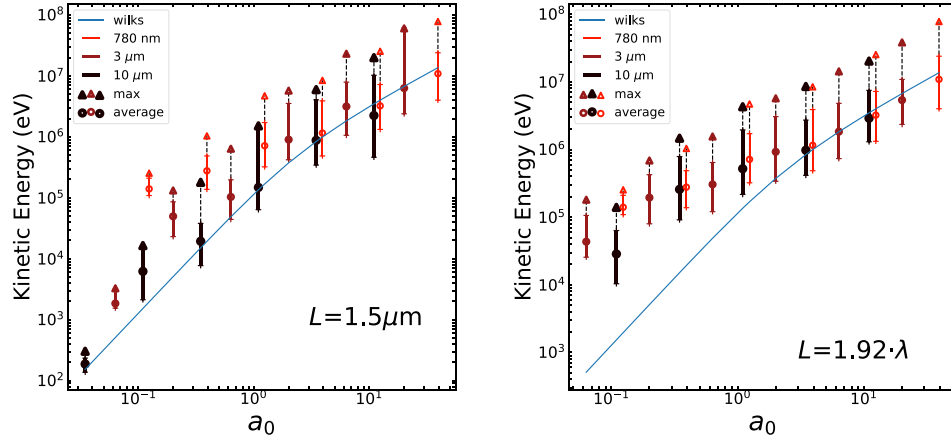


FIG. 1. Left panel: Ejected electron energies observed in PIC simulations with laser wavelengths 780 nm (red), 3 μm (dark red), and 10 μm (black) and with $L = 1.5 \mu\text{m}$. Right panel: Ejected electron measurements from simulations where the pre-plasma scale length is proportional to the wavelength of the laser, such that $L = 1.92 \cdot \lambda$. In both panels, results are shown as a function of a_0 of the incident laser. Expectations from Wilks scaling [Eq. (3)] are shown as a solid blue line. The lowest a_0 case for $L = 1.92 \cdot \lambda$ is not shown, as accelerated electrons were not detected in that case. Open circles represent the mean kinetic energy of accelerated electrons that reach the edge of the simulation space in a 150° apex cone in the backward direction. The error bars represent 68% of the electrons around the mean energy bin. The triangles represent the maximum ejected electron energy observed. Dashed lines connect the triangles to the error bars so that it is easy to see that these measurements come from the same simulation.

For the 780 nm, 3 μm , and 10 μm wavelengths, this corresponds to $n_c = 1.74 \times 10^{21} \text{ cm}^{-3}$, $1.24 \times 10^{20} \text{ cm}^{-3}$, and $1.11 \times 10^{19} \text{ cm}^{-3}$, respectively. In all simulations, the laser focus was chosen to coincide with the critical density in the pre-plasma layer. For the 780 nm simulations, a spatial resolution with a spacing of 33 nm (roughly 23 cells per wavelength) was used and a time-step of 0.1 fs was used. For the 3 μm simulations, a spacing of 100 nm and a temporal resolution of 0.15 fs was used. Finally, the 10 μm simulations utilized a spatial resolution of 250 nm and a temporal resolution of 0.5 fs. Although these simulations do not resolve the Debye length in every cell (since there are cells with near-solid densities with sub-nanometer Debye lengths), the phenomenon of interest is the electron acceleration in the underdense pre-plasma extending from the target where the Debye length is much larger and more easily resolved. The implicit algorithm in LSP avoids grid-heating issues associated with the Debye instability, so that the behavior of near-solid density regions in the simulation does not ruin the overall energy conservation of the simulation. All simulations had 27 macro-particles per cell per species (free electrons, protons, and O^+ ions). As in an earlier work by Orban *et al.*,¹ the O^+ ions in this simulation can be further ionized by strong electric fields according to the Ammisov-Delone-Krainov/Perelomov-Popov-Terentev rate.^{15,16} In the simulation, electron macroparticles scatter by a Monte-Carlo algorithm as in Kemp *et al.*¹⁷ with a scattering rate determined by a Spitzer model,¹⁸ except at low temperatures where the scattering rate is limited by the timestep. The 1.5 μm scale-length simulations were run for three times the duration of the simulated laser pulse (i.e., three times the full-width full maximum duration of the pulse). The proportional scale-length simulations were run for 3.5 times the duration of the simulated laser pulse because these were larger targets with a more extended pre-plasma. The parameters of all simulations are listed in the Appendix, Table II and the parameters common across the given wavelength simulations are summarized in Table I.

III. RESULTS

A. Ejected electron energies

Figure 1 shows the energy spectra of back-accelerated electrons for all the simulations performed. The left panel of Fig. 1 shows the results of the simulations with a 1.5 μm scale-length pre-plasma, while the right panel plots the results of the proportional scale-length simulations where the scale-length is proportional to the wavelength ($L = 1.92\lambda$). These figures plot the mean and maximum energy of escaping electrons on the y-axis as a function of the normalized vector potential a_0 of the incident laser. Here,

$$a_0 = eE_0/m_e\omega c, \quad (2)$$

where the peak electric field value of the incident pulse is denoted E_0 , c is the speed of light, m_e is the mass of an electron, and $\omega = 2\pi c/\lambda$ is the angular frequency of the laser beam. The mean electron energy is determined by taking the average energy of electrons that reach the boundary of the simulation. Since we are concerned here with back-directed electrons, only those electrons with a momentum angle within $\pm 75^\circ$ of the incident laser are counted.

These results are found to scale with the Wilks scaling estimate from¹⁹

$$E_{\text{wilks}} = \left[\sqrt{1 + \frac{1}{2}a_0^2} - 1 \right] m_e c^2. \quad (3)$$

While there are a number of other formulae that describe the typical energy of electrons interacting with an intense laser field, we choose to compare with Wilks scaling because it is an analytically motivated formula that is reasonably representative of various scaling models in this regime.²⁰ The Wilks model also reduces to the classical ponderomotive energy of an electron in a monochromatic plane wave in the low a_0 limit. A binomial approximation yields

$$E_{\text{wilks}} \approx \frac{1}{4} m_e c^2 a_0^2$$

for small values of a_0 , which is the classical ponderomotive energy. This is why, in Fig. 1, one sees an a_0^2 dependence for Eq. (3) at low a_0 that transitions to linear dependence (i.e., $\sim a_0$) for $a_0 \gtrsim 1$.

Comparing Eq. (3) to the simulation data in the left panel of Fig. 1 yields an interesting result that the 10 μm wavelength simulations fall closest to the Wilks scaling model prediction, while the 3 μm and 780 nm wavelength simulations lie significantly above the prediction, especially for low a_0 values. The 780 nm wavelength simulations have the most energetic electrons, exceeding the energies predicted by Eq. (3) $\times 1$ –2 orders of magnitude. Thus, we say that the ejected electrons in the 780 nm simulations are highly “superponderomotive.” The right panel of Fig. 1 shows the results of the proportional scale-length simulations. 780 nm simulations with 1.5 μm scale-length appear in both panels of Fig. 1. Remarkably, all simulations where the L is proportional to λ seem to follow roughly the same trend and exceed the Wilks prediction by 1–2 orders of magnitude.

Figure 2 presents detailed information on the energies and ejection angles of electrons that leave the simulation volume. Figure 2 shows the results from the three different wavelengths, highlighting intensities with $a_0 \sim 1$ and the mid-IR simulations with $L = 1.92\lambda$. We also overplot with

solid lines the results from an analytic model described in Ref. 2. This model considers that the back-directed electrons are ejected at high speed into a pulsed plane wave that approximates the reflected laser pulse. Because of the similarity to earlier work in Ref. 2, it is unsurprising that the model compares favorably to the 780 nm results shown in Fig. 2. What is more remarkable is that the model predictions compare similarly well to the mid-IR simulations.

B. Electron density profiles

Figure 3 provides snapshots of the electron density in the simulation after the reflection of the laser, and while electrons are propagating away from the target (times explained in the caption of Fig. 3). The figure demonstrates that the onset of plasma phenomena is dependent on the a_0 value of the incident laser pulse, and not only on the laser wavelength or laser intensity independently. For $a_0 < 0.2$, for all wavelengths, the escaping electrons are not spatially bunched, and the pre-plasma layer is perturbed less relative to the more intense cases. With a_0 values between 0.2 and 0.4, the backwards accelerated electrons break apart the pre-plasma layer as they escape with higher energies. At near relativistic a_0 values near ~ 0.5 and above, the ejected electrons are energetic enough to co-propagate with the laser, and begin to exhibit a bunching pattern. This pattern becomes more pronounced as a_0 exceeds unity. As discussed in Ref. 1, this arises because electrons are only deflected away from the

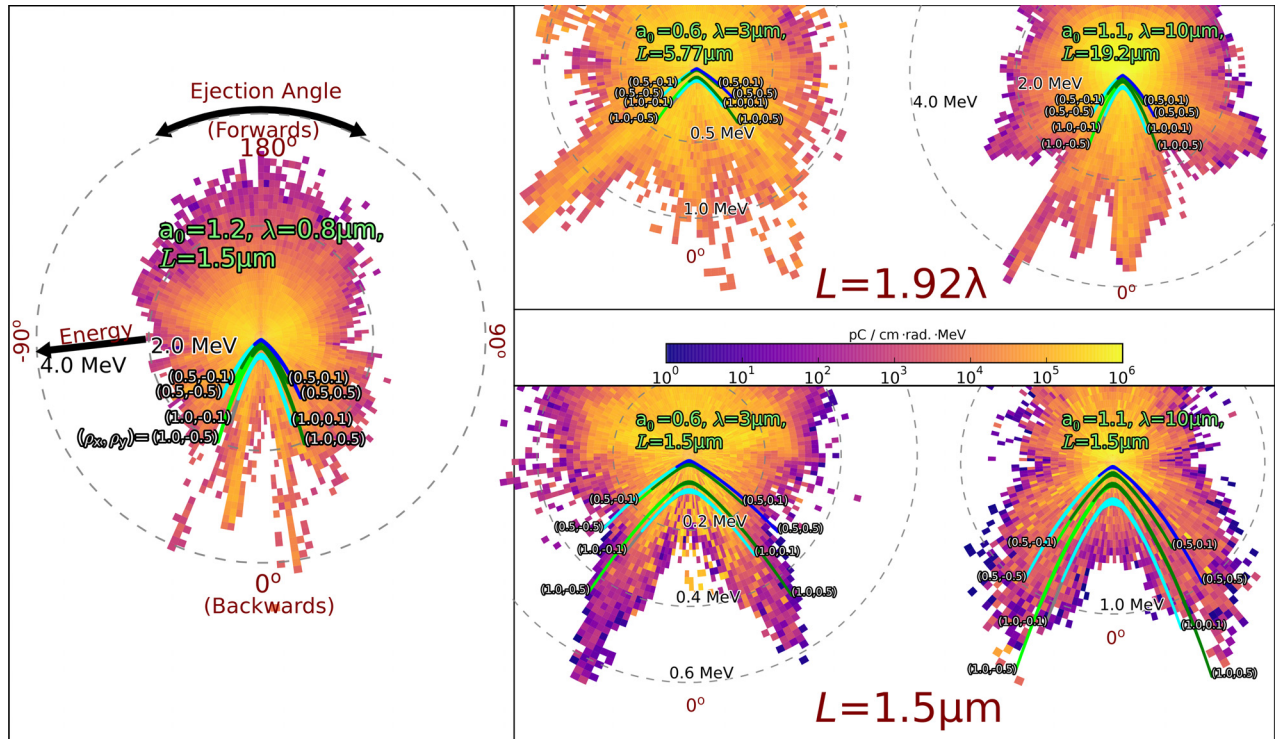


FIG. 2. Summary of kinetic energies and ejection angles of electrons that escape the simulation space of selected PIC simulations in which the incident laser has $a_0 \sim 1$. In all panels, the distance from the center represents the kinetic energy of escaping electrons, while the angle to the origin represents the final ejection angle, and the color is proportional to the amount of charge in a particular energy and angular bin. The left panel shows a 780 nm simulation with $a_0 = 1.2$, while the two simulations in the center column show two different 3 μm simulations with $a_0 = 0.6$ and the right column shows two different 10 μm simulations with $a_0 = 1.1$. The upper right panel shows two mid-IR simulations with an $L = 1.92\lambda$ exponential scale length, while the lower right panel shows two mid-IR simulations with $L = 1.5 \mu\text{m}$. An analytic model from Ref. 2 is overlaid in each panel and labeled by the normalized momentum similar to figures shown in Ref. 2.

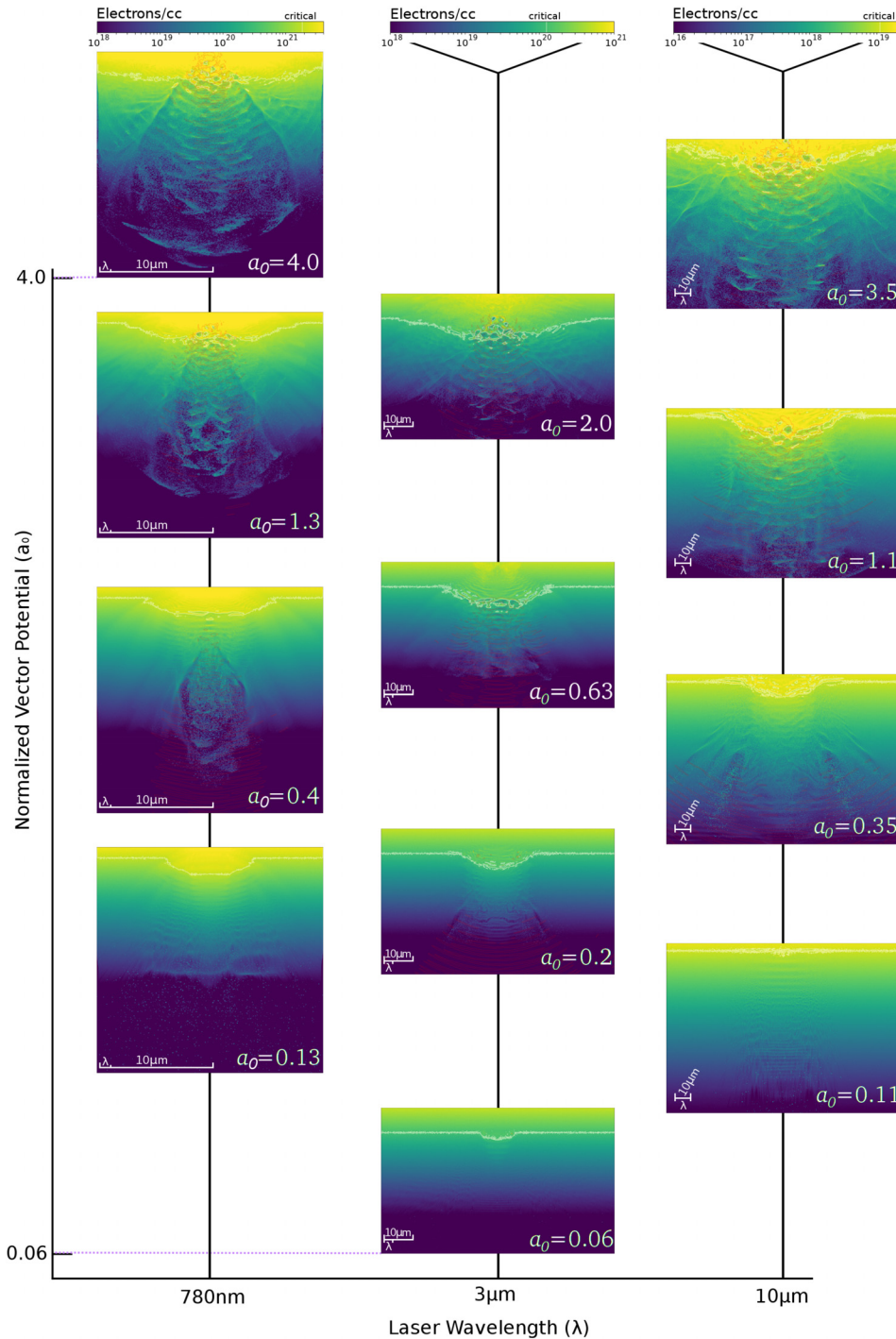


FIG. 3. Electron density snapshots (color mapped rectangles) from twelve unique simulations ranging over wavelengths and a_0 values. Left, middle, and center columns classify the snapshots by the wavelength of the incident laser as 780 nm, 3 μm , and 10 μm , respectively. The vertical axis shows the a_0 value of the incident laser, with the bottom edge of a snapshot aligned with the peak a_0 of the incident laser in that simulation. Color bars (top) and spatial scale bars (within each snapshot) are consistent for each column. The snapshots are taken at times when escaping electrons have propagated well into the backward direction. For $a_0 < 0.2$, the time snapshot is taken at 60 T ; for $0.2 \leq a_0 < 0.5$, the snapshot is taken at 23 T ; and for near-relativistic cases and above ($a_0 > 0.5$), the snapshots are taken at 11 T , where T is the laser period and all times are taken once the peak of the laser reaches the (non-relativistic) critical density surface. For further illustration of the observed plasma phenomena, see the video available online with this article. (Multimedia view) [URL: <http://dx.doi.org/10.1063/1.4995669.1>]

target during two specific moments during the laser cycle. Also, it has been observed that the onset of these bunches is preceded in the process of reflection by a significant electron density hole created by the ponderomotive force, which manifests only as a_0 reaches this regime. As a_0 exceeds 2.0, the laser begins to penetrate beyond the (non-relativistic) critical density surface due to relativistic transparency.²¹ Hole-boring⁷ does not occur in this case due to the ultrashort pulse in all cases, and the laser pulse begins to penetrate only when the last few cycles of the main pulse are present on the non-relativistic critical density surface. To further illustrate this, Fig. 4 compares the Poynting flux for 10 μm simulations with $a_0 = 1.1$ to $a_0 = 3.5$ at similar times, and demonstrates

deeper penetration for the more relativistic a_0 case. Here, reflection occurs closer to the relativistic critical density

$$n_{c,rel} = n_c \gamma \approx n_c \sqrt{1 + \frac{1}{2} a_0^2}, \quad (4)$$

using an estimate for the γ -factor near the reflection point from Eq. (3). Equation (3) suggests that when a_0 exceeds 2.0, the γ -factor exceeds 1.7, representing a more substantial shift from the critical density from Eq. (1). A further illustration of the onset of plasma phenomena that we observe is included as an online video hyperlinked in Fig. 3.

To comment on another aspect of the plots in Fig. 3, in essentially all of the plots shown ($0.06 < a_0 < 4$) the laser

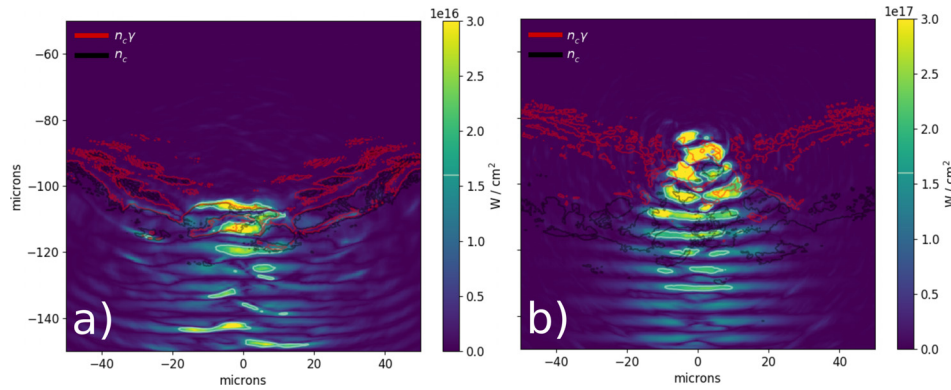


FIG. 4. Norm of Poynting vector flux for $10\ \mu\text{m}$, proportional scale-length simulations, showing a deeper penetration into the target as a_0 increases beyond 2.0. The left panel (a) shows $a_0 = 1.1$ and the right panel (b) shows $a_0 = 3.5$. Highlighted in red is an estimate of the relativistic critical density defined in Eq. (4) and in black is the non-relativistic critical density from Eq. (1). On both plots, the peak intensity of the laser is highlighted in white. Similar features are observed for other wavelength simulations. Both snapshots are taken at $3T$ after the peak of the pulse reaches the non-relativistic critical density.

ionizes the target, moving the critical density (white contour) towards the incoming laser, especially along the laser axis. Because the laser intensity decreases away from the laser axis according to a Gaussian spatial profile, this causes the critical density to assume a curved shape as seen in the figure.

C. Ponderomotive steepening

While Fig. 3 demonstrates that the onset of plasma phenomena is determined by the a_0 value of the incident laser corresponding to the trend across the vertical axis, it also demonstrates that at a given a_0 , the plasma features observed scale in physical size with the incident laser wavelength, which is seen across the horizontal axis. One can take advantage of this scaling of the laser plasma interaction to facilitate the experimental observation of phenomena which would not be observable with shorter wavelength lasers.

One such phenomenon is ponderomotive steepening, which is a well-known laser-plasma interaction process where the radiation pressure from the laser modifies the electron density profile, which, over time, will substantially modify the ion density profile²² on the scale of half the wavelength. A related process is “hole boring” which has been studied theoretically and experimentally (e.g., Ref. 7, and references therein). Unlike hole boring, ponderomotive steepening, as originally described by Ref. 22, creates a series of peaks in the ion density profile. Ponderomotive steepening has been observed in a number of PIC simulations in the literature [e.g., 1]. However, to the best of our knowledge, ponderomotive steepening has never been experimentally observed because the size of such features would be on the sub-micron scale for near IR and optical lasers. To be able to see this phenomenon, one needs an intense laser and high spatial resolution interferometry of the target that can resolve half-wavelength-scale features. Mid-IR lasers, therefore, significantly relax the spatial resolution requirements of such an experiment compared to lasers in the near-IR.

With this in mind, we looked for ponderomotive steepening in our simulations and found these features for simulations, where a_0 is near unity. The $3\ \mu\text{m}$ wavelength

simulation with $a_0 = 0.6$ and $L = 5.77\ \mu\text{m}$ and the $10\ \mu\text{m}$ wavelength simulation with $a_0 = 1.09$ and $L = 19.2\ \mu\text{m}$ specifically exhibit a classic ponderomotive steepening pattern with multiple peaks in both the ion and the electron density as shown in Fig. 5. Ponderomotive steepening was noticed earlier in 800 nm wavelength simulations presented in Ref. 1, c.f. Fig. 12. Ponderomotive steepening was also present in the 3D PIC simulations of near-IR-laser interactions that we published in Ref. 2, although for brevity, we did not highlight this result. Figure 5 provides essentially the first compelling evidence that this effect should persist in mid-IR experiments of this kind.

IV. DISCUSSION

We present 30 high-resolution PIC simulations, which comprise a parameter scan over laser wavelengths, intensities, and target scale-lengths, designed to explore the physics of intense, normally-incident near-IR (780 nm wavelength) and mid-IR ($3\ \mu\text{m}$ and $10\ \mu\text{m}$ wavelength) laser-plasma interactions in the creation of superponderomotive electrons. The simulations support three major findings. The first major conclusion is that the backward acceleration of electrons in the sub-relativistic regime is much more efficient when the scale-length L of the pre-plasma is similar to or longer than the wavelength λ ($L/\lambda \gtrsim 1$). Second, the onset of plasma phenomenon scales with the a_0 value of the incident pulse, which, of course, takes contributions from both the intensity of the incident light and its wavelength. Finally, the physical scale of plasma phenomena scales with the wavelength, facilitating the experimental observation of features such as ponderomotive steepening.

The importance of the condition $L/\lambda \gtrsim 1$ is seen from comparing the energies of near-IR and mid-IR simulations with similar a_0 values and scale lengths determined by $L = 1.92\lambda$, shown on the right panel of Fig. 1 to those of simulations with similar a_0 values on the left panel with a fixed scale length $L = 1.5\ \mu\text{m}$. In the sub-relativistic regime ($a_0 \ll 1$), we find that the proportional scale length simulations with $L = 1.92\lambda$ produce ejected electrons that lie well above expectations from Ref. 19. Moreover, from examining just the simulations with a fixed $L = 1.5\ \mu\text{m}$, one finds that

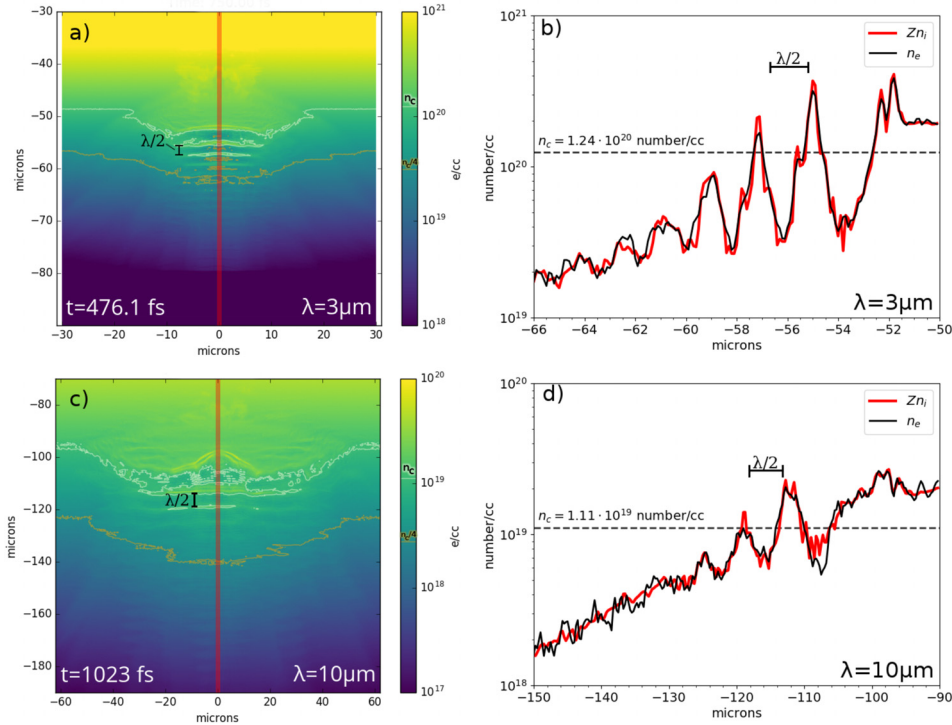


FIG. 5. Panel (a) shows a 2D pseudo-color of ion charge density, i.e., Zn_i , where Z is the mean charge state of the plasma and n_i is the ion density, in the sub-critical pre-plasma region for a $3\text{ }\mu\text{m}$ wavelength simulation with a $6.08 \times 10^{16}\text{ W/cm}^2$ laser pulse ($a_0 = 0.6$). The pulse is incident on a proportional scale-length pre-plasma target ($L = 5.77\text{ }\mu\text{m}$). Panel (b) shows a central line out of the ion charge density (red) and electron density (black), with the lineout taken from the highlighted red line in (a). The bottom rows [panels (c) and (d)] are similar plots for a $10\text{ }\mu\text{m}$ wavelength simulation with a $1.64 \times 10^{16}\text{ W/cm}^2$ laser pulse. The displayed snapshots show the target state well after the laser reflection has left the simulation space. On panels (a) and (c), the charge density equivalent to critical electron density is highlighted with white contours, and the quarter of critical electron density is highlighted with an orange contour. In all panels, the spatial scale of $\lambda/2$ is labeled, given its relevance to ponderomotive steepening as described in Ref. 22. The time indicated corresponds to the time since the peak of the laser has reached the (non-relativistic) critical density surface.

longer wavelength simulations tend to produce less energetic electrons than shorter wavelength simulations. These longer wavelength cases represent values of $L/\lambda = 0.5, 0.15$ for $\lambda = 3\text{ }\mu\text{m}, 10\text{ }\mu\text{m}$, respectively. This further reinforces the idea that the L/λ ratio needs to be unity or greater for back-directed electron acceleration to be effective in the low a_0 regime.

The Wilks scaling estimate is linear in a_0 in the regime where $a_0 > 1$ and quadratic in a_0 in the non-relativistic case ($a_0 < 1$), as discussed earlier. The scaling of energies for backward accelerated electrons for the simulations with an extended pre-plasma $L/\lambda = 1.92$ appears to follow a linear power law that extends below the non-relativistic limit at $a_0 \sim 1$ and thus exceed the classical ponderomotive scaling in the sub-relativistic regime, demonstrated by the bifurcation of the Wilks scaling and the trend for backward-accelerated electrons at $a_0 \sim 1$ on the right panel of Fig. 1. As mentioned in the caption of that figure, the lowest a_0 simulation did not have accelerated electrons that reached the edge of the simulation space by the end of the simulation, so it is doubtful that this power law extends to a_0 values well below 10^{-1} . This lower energy regime will be the focus of future work.

We further highlight the difference between the $L = 1.5\text{ }\mu\text{m}$ and the proportional scale-length $L = 1.92\lambda$ cases by examining in Fig. 2 the ejected electron energy and the angle spectra for a set of simulations with similar a_0 values. The

angle spectra for the $1.5\text{ }\mu\text{m}$ scale-length simulations (bottom panel) match the analytical model from Ref. 2 more closely than the $L = 1.92\lambda$ results (upper panel) do, and they are quite a bit more energetic than expected from the model, and the $L = 1.92\lambda$ simulations have a larger amount of total charge accelerated compared to the $L/\lambda < 1$ cases (lower panel). As explained in Ref. 2, the analytic model to which we compare is purely electromagnetic and does not include plasma effects which become more prominent as the ratio L/λ increases and the volume of near-critical density plasma becomes larger.

A number of reasons could explain why the ratio L/λ is important for electron acceleration. It is well known that intense laser interactions are highly sensitive to the assumed scale length; from a physics perspective (c.f. Ref. 23), one expects that if $L/\lambda \ll 1$, then the laser will reflect off a sharp interface (much like a mirror) and only accelerate electrons that reside on the surface of the target. If instead $L/\lambda \gtrsim 1$, then the laser will interact with a more extended region of near-critical plasma, as we mentioned earlier, and that provides a more suitable environment for accelerating large numbers of electrons in the *backward* direction. It should also be emphasized that the proportional scale-length targets are significantly longer longitudinally than the $L = 1.5\text{ }\mu\text{m}$ targets, and also provide a larger return current in the path of the escaping electrons. These are the possible explanation for both the increased energy for the simulations where $L =$

1.92λ and the larger number of ejected electrons, as discussed earlier and shown in Figs. 1 and 2. Finally, the ratio L/λ is relevant especially in the sub-relativistic regime ($a_0 < 1$), and as discussed in Sec. III B and Fig. 3, different plasma phenomena are observed across different a_0 regimes. These effects, relevant mechanisms, as well as the confluence of the a_0 value with the ratio L/λ , will be investigated in future work.

Finally, as discussed in Secs. III B and III C and shown in Fig. 5, we anticipated the scaling of plasma features with the size of the incident laser wavelength, and observed ponderomotive steepening in the longer wavelength IR simulations with $a_0 \sim 1$ and found multiple peaks in the density distribution. While it is out of scope of this paper to design in detail a mid-IR experiment that would create these conditions and convincingly detect these density modulations using interferometry, the result is very encouraging from an experimental perspective. We comment here to say that (1) high-resolution interferometric systems have been demonstrated with soft X-ray wavelengths and used productively for research (e.g., Ref. 24) and (2) high repetition rate laser experiments with rapidly recovering, highly-reproducible liquid targets can potentially be used with a high acquisition rate interferometric system (e.g., Ref. 25) to study how these features develop over time.

V. CONCLUSIONS

In anticipation of future experiments utilizing ultra-intense, mid-infrared laser pulses and their interaction with dense targets, we used LSP 2D(3v) simulations to explore these interactions over a range of intensities and wavelengths. Similar to earlier investigations with near-IR light,^{1,2} we find that intense mid IR wavelength interactions also produce highly superponderomotive electrons. Moreover, the acceleration is much more effective when the

pre-plasma scale length is in similar scale to the laser wavelength, or longer. In some cases, the typical ejected electron energies exceed ponderomotive expectations by orders of magnitude.

The larger wavelength IR simulations also indicate that ponderomotive steepening should occur in experiments of this kind when $a_0 \sim 1$ and the pre-plasma scale length is again similar in scale to the laser wavelength. This likewise extends earlier results in the near-IR,¹ where this phenomena was noticed in simulations. Importantly, ponderomotive steepening can create multiple peaks and valleys in the ion and electron density profile in the pre-plasma that are well known to be spaced by $\lambda/2$ peak-to-peak. To our knowledge, these density modulations have never been observed experimentally. Intense mid-IR laser systems coupled with high-resolution interferometry techniques should provide a promising venue for demonstrating this basic laser-plasma interaction process.

ACKNOWLEDGMENTS

This research was sponsored by the Air Force Office of Scientific Research (AFOSR) through program managers Dr. Enrique Parra and Dr. Jean-Luc Cambier. The authors acknowledge significant support from the Department of Defense High Performance Computing Modernization Program (DOD HPCMP) Internship Program and the AFOSR summer faculty program. Supercomputer time was used on the DOD HPC Armstrong and Garnet supercomputers. The authors would also like to thank The Ohio State Department of Physics Information Technology support, specifically, Keith A. Stewart. We also thank Tan Hui Yi in her help in producing a video for this paper.

APPENDIX A: EXHAUSTIVE LIST OF SIMULATIONS

TABLE II. Summary of parameters of all the 2D(3v)/LSP PIC simulations performed sorted according to the value of a_0 for each simulation.

Wavelength (μm)	Intensity (W/cm^2)	a_0	Gaussian radius (μm)	Pulse FWHM (fs)	Laser energy (J)	Pre-plasma scale (μm)	Target density (cm^{-3})	Simulation timestep (fs)	Simulation spatial resolution (μm)
10	1.64×10^{13}	0.0346	27.5	513	10^{-4}	1.5	10^{23}	0.5	0.25
10	1.64×10^{13}	0.0346	27.5	513	10^{-4}	19.2	10^{21}	0.5	0.25
3	6.08×10^{14}	0.0632	8.25	154	10^{-4}	1.5	10^{23}	0.15	0.1
3	6.08×10^{14}	0.0632	8.25	154	10^{-4}	5.77	10^{23}	0.15	0.1
10	1.64×10^{14}	0.109	27.5	513	10^{-3}	1.5	10^{23}	0.5	0.25
10	1.64×10^{14}	0.109	27.5	513	10^{-3}	19.2	10^{21}	0.5	0.25
0.78	3.46×10^{16}	0.124	2.15	40	10^{-4}	1.5	10^{23}	0.1	0.033
3	6.08×10^{15}	0.200	8.25	154	10^{-3}	1.5	10^{23}	0.15	0.1
3	6.08×10^{15}	0.200	8.25	154	10^{-3}	5.77	10^{23}	0.15	0.1
10	1.64×10^{15}	0.346	27.5	513	10^{-2}	1.5	10^{23}	0.5	0.25
10	1.64×10^{15}	0.346	27.5	513	10^{-2}	19.2	10^{21}	0.5	0.25
0.78	3.46×10^{17}	0.392	2.15	40	10^{-3}	1.5	10^{23}	0.1	0.033
3	6.08×10^{16}	0.632	8.25	154	10^{-2}	1.5	10^{23}	0.15	0.1
3	6.08×10^{16}	0.632	8.25	154	10^{-2}	5.77	10^{23}	0.15	0.1
10	1.64×10^{16}	1.09	27.5	513	10^{-1}	1.5	10^{23}	0.5	0.25
10	1.64×10^{16}	1.09	27.5	513	10^{-1}	19.2	10^{21}	0.5	0.25
0.78	3.46×10^{18}	1.24	2.15	40	10^{-2}	1.5	10^{23}	0.1	0.033
3	6.08×10^{17}	2.00	8.25	154	10^{-1}	1.5	10^{23}	0.15	0.1

TABLE II. (Continued.)

Wavelength (μm)	Intensity (W/cm^2)	a_0	Gaussian radius (μm)	Pulse FWHM (fs)	Laser energy (J)	Pre-plasma scale (μm)	Target density (cm^{-3})	Simulation timestep (fs)	Simulation spatial resolution (μm)
3	6.08×10^{17}	2.00	8.25	154	10^{-1}	5.77	10^{23}	0.15	0.1
10	1.64×10^{17}	3.46	27.5	513	1	1.5	10^{23}	0.5	0.25
10	1.64×10^{17}	3.46	27.5	513	1	19.2	10^{21}	0.5	0.25
0.78	3.46×10^{19}	3.92	2.15	40	10^{-1}	1.5	10^{23}	0.1	0.033
3	6.08×10^{18}	6.32	8.25	154	1	1.5	10^{23}	0.15	0.1
3	6.08×10^{18}	6.32	8.25	154	1	5.77	10^{23}	0.15	0.1
10	1.64×10^{18}	10.9	27.5	513	10	1.5	10^{23}	0.5	0.25
10	1.64×10^{18}	10.9	27.5	513	10	19.2	10^{21}	0.5	0.25
0.78	3.46×10^{20}	12.4	2.15	40	1	1.5	10^{23}	0.1	0.033
3	6.08×10^{19}	20.0	8.25	154	10	1.5	10^{23}	0.15	0.1
3	6.08×10^{19}	20.0	8.25	154	10	5.77	10^{23}	0.15	0.1
0.78	3.46×10^{20}	39.2	2.15	40	10	1.5	10^{23}	0.1	0.033

¹C. Orban, J. T. Morison, E. D. Chowdhury, J. A. Nees, K. Frische, and W. M. Roquemore, *Phys. Plasmas* **22**, 023110 (2015).

²G. K. Ngirmang, C. Orban, S. Feister, J. T. Morrison, K. D. Frische, E. A. Chowdhury, and W. M. Roquemore, *Phys. Plasmas* **23**, 043111 (2016).

³See Mid-ir lasers: Power and pulse capability ramp up for mid-ir lasers for <http://www.laserfocusworld.com/articles/print/volume-50/issue-05/features/mid-ir-lasers-power-and-pulse-capability-ramp-up-for-mid-ir-lasers.html>; accessed 1 January 2017.

⁴See Muri mid-infrared strong-field interaction for <http://muri-mir.osu.edu>; accessed 1 January 2017.

⁵T. Elder and J. Strong, *J. Franklin Inst.* **255**, 189 (1953).

⁶See Muri mid-infrared strong-field interaction, research thrusts for <http://muri-mir.osu.edu/node/13/###research>; accessed 1 January 2017.

⁷C. Gong, S. Y. Tochitsky, F. Fiuza, J. J. Pigeon, and C. Joshi, *Phys. Rev. E* **93**, 061202 (2016).

⁸A. V. Mitrofanov, A. A. Voronin, D. A. Sidorov-Biryukov, A. Puglyis, E. A. Stepanov, G. Andriukaitis, T. Flry, S. Aliauskas, A. B. Fedotov, A. Baltuka *et al.*, *Scientific Reports* **5**, 8368 (2015).

⁹D. R. Austin, K. R. P. Kafka, S. Trendafilov, G. Shvets, H. Li, A. Y. Yi, U. B. Szafruga, Z. Wang, Y. H. Lai, C. I. Blaga *et al.*, *Opt. Express* **23**, 19522 (2015).

¹⁰D. R. Austin, K. R. P. Kafka, Y. H. Lai, Z. Wang, K. Zhang, H. Li, C. I. Blaga, A. Y. Yi, L. F. DiMauro, and E. A. Chowdhury, *J. Appl. Phys.* **120**, 143103 (2016).

¹¹J. T. Morrison, E. A. Chowdhury, K. D. Frische, S. Feister, V. M. Ovchinnikov, J. A. Nees, C. Orban, R. R. Freeman, and W. M. Roquemore, *Phys. Plasmas* **22**, 043101 (2015).

¹²S. Feister, D. R. Austin, J. T. Morrison, K. D. Frische, C. Orban, G. Ngirmang, A. Handler, J. R. H. Smith, M. Schillaci, J. A. LaVerne *et al.*, *Opt. Express* **25**, 18736 (2017).

¹³D. Haberberger, S. Tochitsky, and C. Joshi, *Opt. Express* **18**, 17865 (2010).

¹⁴D. R. Welch, D. V. Rose, R. E. Clark, T. C. Genoni, and T. P. Hughes, *Comput. Phys. Commun.* **164**, 183 (2004).

¹⁵M. Ammosov, N. B. Delone, and V. P. Krainov, *Sov. Phys. JETP* **64**, 1191 (1986).

¹⁶A. Perelomov, V. Popov, and M. Terentev, *Zh. Eksp. Teor. Fiz.* **50**, 1393 (1966).

¹⁷A. J. Kemp, R. E. W. Pfund, and J. Meyer-Ter-Vehn, *Phys. Plasmas* **11**, 5648 (2004).

¹⁸L. Spitzer, *Am. J. Phys.* **31**, 890 (1963).

¹⁹S. C. Wilks, W. L. Kruer, M. Tabak, and A. B. Langdon, *Phys. Rev. Lett.* **69**, 1383 (1992).

²⁰F. N. Beg, A. R. Bell, A. E. Dangor, C. N. Danson, A. P. Fewes, M. E. Glinsky, B. A. Hammel, P. Lee, P. A. Norreys, and M. Tatarakis, *Phys. Plasmas* **4**, 447 (1997).

²¹S. Palaniyappan, B. M. Hegelich, H.-C. Wu, D. Jung, D. C. Gautier, L. Yin, B. J. Albright, R. P. Johnson, T. Shimada, S. Letzring *et al.*, *Nat. Phys.* **8**, 763 (2012).

²²K. Estabrook and W. L. Kruer, *Phys. Fluids* **26**, 1888 (1983).

²³P. Gibbon, *Short Pulse Laser Interactions with Matter: An Introduction* (Imperial College Press, 2005).

²⁴J. Grava, M. A. Purvis, J. Filevich, M. C. Marconi, J. J. Rocca, J. Dunn, S. J. Moon, and V. N. Shlyaptsev, *Phys. Rev. E* **78**, 016403 (2008).

²⁵S. Feister, J. A. Nees, J. T. Morrison, K. D. Frische, C. Orban, E. A. Chowdhury, and W. M. Roquemore, *Rev. Sci. Instrum.* **85**, 11D602 (2014).